Nonlinear Baroclinic Adjustment and Wavenumber Selection in a Simple Case

Wendell T. Welch

National Center for Atmospheric Research,* Advanced Study Program, Boulder, Colorado

Ka-Kit Tung

Department of Applied Mathematics, University of Washington, Seattle, Washington

ABSTRACT

The process of baroclinic equilibration in the atmosphere is investigated using a high-resolution two-layer quasigeostrophic model in a β-plane channel. One simple channel geometry is investigated for which only two zonal waves are initially unstable, with the shorter being linearly more unstable but nonlinearly less effective. It is discovered that the mechanism of nonlinear baroclinic adjustment, formerly proposed by Cehelsky and Tung, including a nonlinear wavenumber selection process, can explain the equilibration at all levels of forcing for this case. At small forcings the most unstable wave dominates the heat flux, consistent with the quasi-linear equilibration of Stone's simple baroclinic adjustment. At high forcings the longer, less unstable wave dominates, and the equilibration involves both quasi-linear dynamics by this dominant wave and nonlinear transfer from the shorter to the longer wave. For intermediate forcings there is a transition between the low and high regimes; no single wave dominates.

At every forcing except in the intermediate regime there is critical equilibration by the dominant wave. For intermediate forcings, the model equilibrates at a value between the critical shear of the two waves.

The wavenumber selection process involves a threshold of heat transport for each wave. Above this, the amplitude of the wave would be so large as to cause itself to break and saturate. The shorter wave's threshold occurs at moderate forcings, at which point it relinquishes dominance to the longer wave. A method for calculating these thresholds is proposed, which involves only robust features of the equilibrium.

1. Introduction

Meridional heat transport in the atmosphere has not yet been accurately simulated in large numerical models (Manabe and Stouffer 1988; Washington and Meehl 1989; Stone and Risbey 1990; Manabe et al. 1991; Cubasch et al. 1993; Maier-Reimer et al. 1993; Manabe and Stouffer 1993). It is known that atmospheric meridional heat transport must be "flexible," that is, highly sensitive to forcing, for, although the radiatively forced meridional temperature gradient varies substantially with the seasons, the observed temperature gradient in midtroposphere remains relatively constant in the course of a year (Stone 1978). Changes in the forcing are reflected as changes in the amount of heat fluxed poleward, while the resultant temperature gradient appears relatively insensitive to the forcing.

One explanation of this effect was proposed by Stone (1978) and elaborated upon by Cehelsky and Tung (1991): the baroclinic adjustment mechanism. Whenever the meridional temperature gradient exceeds a certain "critical" value, baroclinic eddies are enhanced and their effect is to reduce the temperature gradient. This negative feedback between baroclinic eddy heat flux and the meridional temperature gradient thus maintains the gradient at this threshold value. Stone found that a simple approximation for the threshold is the critical temperature gradient from a linear stability analysis of a two-layer model of the atmosphere.

Several authors presented results that did not accord with Stone's theory, however. In their investigations of geostrophic turbulence, Salmon (1980) and Vallis (1988) used fully nonlinear models with many unstable waves and ran them to statistical equilibrium. They found that the ensemble average vertical shear was appreciably higher at equilibrium than the minimum critical shear from a linear stability analysis of the original zonal mean flow, a condition which they term "supercritical equilibration." Furthermore, implicit in Stone's mechanism is the assumption that the linearly most unstable wave captured by his two-level model performs the heat transport. Results from weakly nonlinear cal-

1285

culations (Hart 1981; Pedlosky 1981), fully nonlinear numerical simulations (Gall et al. 1979; Haidvogel and Held 1980; Klein and Pedlosky 1986; Cehelsky and Tung 1991; Whitaker and Barcilon 1995), and observations (Gall 1976; Randel and Held 1991) have shown, however, that at high enough forcing a shift from the system's most unstable wave to a longer, less unstable wave occurs, so that this longer wave dominates at equilibrium.

Cehelsky and Tung (1991) proposed the theory of "nonlinear baroclinic adjustment" to address both of these issues. They suggested that the meridional temperature gradient is maintained at the critical gradient, not necessarily of the most unstable wave but of the dominant heat transporting wave, and they showed this to be true at various forcings from model output. Thus "critical" in the lexicon of nonlinear baroclinic adjustment is defined with respect to whichever wave dominates the heat transport. A flow might seem "supercritical," that is, relative to the most unstable wave, but relative to the dominant heat transporting wave it should be just at critical. In addition, Cehelsky and Tung demonstrated that, as thermal forcing is increased, the dominant heat transporting wave shifts to a larger and larger scale so that at high forcings it is the longest wave allowed by the model geometry that dominates.

Still at issue is what determines which wavenumber will dominate the heat flux and, in particular, which wave dominates for low and moderate forcings. Cehelsky and Tung (1991) did not investigate how the most unstable wave becomes "saturated" and how the shift in dominance occurs. This wavenumber selection mechanism must be nonlinear in that linear and quasi-linear theories are insufficient in explaining its behavior (Salmon 1980; Mak 1985; Vallis 1988; Cehelsky and Tung 1991). There have been several methods suggested to justify which zonal mode dominates at various levels of forcing. Cai (1992) proposed using a quasi-linear model, comparing analytic calculations of equilibrium with different waves perturbed. For each forcing separately he selected that wave which, when perturbed, yielded the lowest equilibrated vertical shear, and he stated that this wave would be dominant in a fully nonlinear simulation at equilibrium. Cai showed that his quasi-linear prediction is correct, but only for low forcings. In fact, at his highest drivings the quasi-linear equilibria are starting to diverge from their nonlinear counterparts. Equilibration of baroclinic flows becomes more complicated as the forcing is increased and the dominance shifts to a wave longer than the most unstable (Cehelsky and Tung 1991). Weakly nonlinear calculations (Hart 1981; Pedlosky 1981) can partially explain this shift, but they usually deal only with low forcings and cases with restricted wave–wave interactions. In addition, such studies do not offer predictions of which wave will dominate.

Whitaker and Barcilon (1995) showed which wave dominates at equilibrium for a large range of parameter values. They pointed out two distinct wave bands: long Rossby waves, which gain energy primarily through an upscale nonlinear energy cascade, and shorter baroclinic waves, which gain energy mostly through quasi-linear extraction from the mean flow. It is a wave at the transition between these two bands that is the most energetic at equilibrium. They demonstrated that for much of parameter space this wave is longer than the most unstable wave and that the most unstable is drained of energy by large nonlinear transfer to longer waves. Their discussion was primarily diagnostic, however. They did not offer a mechanistic explanation of wavenumber selection: how the nonlinear transfer out of the most unstable wave is initiated and why such nonlinearities draw energy from the most unstable wave but not the longer waves. As of yet, no method has been suggested that can explain how the wavenumber selection mechanism works in general and hence predict which wave will dominate at equilibrium for *any* level of forcing.

In this work we investigate baroclinic equilibration using a high-resolution two-layer quasigeostrophic model in a β-plane channel. Although a two-layer model cannot simulate the real atmosphere properly, there is a correspondence between linear stability analysis of a two-layer model and tropospheric observations: the critical gradient in the former corresponds to the cutoff in the atmosphere between shallow waves, ineffective at transporting heat, and long deep waves that can efficiently flux heat poleward (Held 1978). Furthermore, the short (hence shallow) waves that are unresolved in our model do not, by this same argument, contribute significantly to the poleward heat transport, and thus their absence is not important. We use such a simplified model to investigate the qualitative features of meridional heat transport. One specific channel geometry (i.e., aspect ratio) is selected such that only two zonal modes are initially linearly unstable. This is the simplest case that allows for nonlinear interaction of unstable modes. With only two modes to consider, we can analyze the mechanisms of wave energy transfer and wave saturation clearly.

In our model we hold static stability constant in time. However, an important process in equilibrating baroclinic flows, in addition to the reduction of the horizontal temperature gradient, is the adjustment of the vertical temperature profile via vertical eddy heat flux (Gutowski et al. 1989; Zhou and Stone 1993). Here we neglect this effect in order to focus on the interaction of horizontal heat transport and the horizontal temperature profile, consistent with the quasigeostrophic formulation adopted. In the future our results should be tested with a model that allows for variation of the static stability.

In section 2 the mathematical model and its numerical solution is described. Section 3 presents a conceptual model of the full nonlinear baroclinic adjustment mechanism for a wide range of forcings and one simple channel geometry. It is then corroborated with output from the numerical model. Wavenumber selection is dis-

cussed in section 4. A mechanism is proposed for the selection of which wave(s) will dominate at equilibrium, and the process of wave breaking is described. Sections 5 and 6 document additional features of the model results, and finally a summary and conclusions are included in section 7.

2. The numerical model

a. Mathematical formulation

The two-layer model used here is based on the baroclinic quasigeostrophic equations on a β plane, including Newtonian cooling to a radiative equilibrium temperature profile and Ekman damping:

$$\frac{\partial}{\partial t}\nabla^2\Psi = -J(\Psi, \nabla^2\Psi + f) + f_0\frac{\partial\omega}{\partial p} \quad (2.1)$$

$$\frac{\partial}{\partial t}\frac{\partial\Psi}{\partial p} = -J\left(\Psi, \frac{\partial\Psi}{\partial p}\right) - \frac{\sigma}{f_0}\omega - h_d'\left[\frac{\partial\Psi}{\partial p} - \left(\frac{\partial\Psi}{\partial p}\right)^\dagger\right]. \quad (2.2)$$

This formulation was originated by Lorenz (1960) (see also Lorenz 1963; Holton 1979; Cehelsky and Tung 1991). Here x is the longitudinal position, y the latitudinal position on a β plane centered at latitude ϕ_0, p the pressure (the vertical coordinate), and t the time; Ψ is the geostrophic streamfunction, defined in terms of the geopotential via $\Psi = \Phi/f_0$; $\omega = dp/dt$ is the vertical velocity; $J(g_1, g_2) = (\partial g_1/\partial x)(\partial g_2/\partial y) - (\partial g_1/\partial y)(\partial g_2/\partial x)$ the Jacobian; $f = f_0 + \beta_0 y$ the Coriolis parameter; $\sigma = -(\partial\theta_0/\partial p)/(\rho\theta_0)$ a measure of static stability (where θ_0 is a base state potential temperature, assumed not to change); and h_d' a coefficient of Newtonian cooling. A † indicates radiative equilibrium forcing.

The model is restricted to a midlatitude channel centered at $\phi_0 = 50°$N, with a width of 45°. The two layers of fluid exist on top of an Ekman layer, which determines the lower boundary condition of the model (see section 2b). The vorticity equation (2.1) is applied within each layer and the thermodynamic energy equation (2.2) at their interface. This model is the simplest possible that allows for the physics of dry baroclinic heat transport.

The equations are nondimensionalized as follows (carets indicate nondimensional variables): $\hat{x} = x/L_x$, $\hat{y} = y/L_y$, $\widehat{\delta p} = \delta p/\Delta p$, $\hat{t} = tf_0$, $\hat{\Psi} = \Psi/(L_y^2 f_0)$, and $\hat{\omega} = \omega/(f_0\Delta p)$. Here L_x and L_y are representative horizontal length scales and Δp is the pressure difference between model levels 1 and 3. Magnitudes of scaling quantities are given in section 2c. Note that we use only a Coriolis timescale f_0 and no advective timescale. This yields small nondimensional velocities, for example, $O(0.1)$ in the upper troposphere, but dimensionally these velocities agree with observed magnitudes and there is no inconsistency in the method.

After dropping the carets, the nondimensional layered equations are

$$\frac{\partial}{\partial t}\nabla^2_\delta\Psi_1 = -\delta J(\Psi_1, \nabla^2_\delta\Psi_1) - \delta\beta\frac{\partial\Psi_1}{\partial x} + \omega_2 - \omega_0 \quad (2.3)$$

$$\frac{\partial}{\partial t}\nabla^2_\delta\Psi_3 = -\delta J(\Psi_3, \nabla^2_\delta\Psi_3) - \delta\beta\frac{\partial\Psi_3}{\partial x} + \omega_4 - \omega_2 \quad (2.4)$$

$$\frac{\partial}{\partial t}(\Psi_3 - \Psi_1) = -\frac{1}{2}\delta J(\Psi_1 + \Psi_3, \Psi_3 - \Psi_1) - 2\sigma_0\omega_2$$
$$-2h''[\Psi_3 - \Psi_1 - (\Psi_3 - \Psi_1)^\dagger], \quad (2.5)$$

where subscripts 1 and 3 indicate the upper and lower layers, 2 the interface, and 0 and 4 the top and bottom of the model, respectively. Several nondimensional parameters have been introduced: $\beta \equiv L_y\beta_0/f_0$, $\sigma_0 \equiv (\Delta p)^2\sigma/(2L_y^2 f_0^2)$, $h'' \equiv h_d'/(2f_0)$, and $\delta \equiv L_y/L_x$; δ is a horizontal aspect ratio.[1] Here $\nabla^2_\delta = \delta^2(\partial^2/\partial x^2) + (\partial^2/\partial y^2)$ is the nondimensionalized Laplacian operator. For more details of the model, see Welch (1996) and Cehelsky (1987).

b. Boundary conditions

Boundary conditions in x are periodic, and in y we assume rigid walls, which is equivalent to no zonal momentum convergence at the walls (Phillips 1954). In p we assume a rigid lid at the top, $\omega_0 = 0$, and at the bottom ω_4 equals the vertical velocity coming out of the underlying Ekman layer. This velocity has two parts: that due to Ekman pumping and that due to topographical uplift (Tung 1983). The Ekman pumping velocity is proportional to the geostrophic vorticity of the bulk fluid: $\omega_4 \sim -\zeta_g$ (Holton 1979). Applying this to the lower layer yields $\omega_4 = -2\nu\nabla^2_\delta\Psi_4$, which we approximate by $\omega_4 \approx -2\nu\nabla^2_\delta\Psi_3$ where ν is a coefficient of Ekman damping. (The "2" is added in analogy with the thermal damping term.) This last approximation is tested and discussed in section 6. In this study we will omit topography to isolate the behavior of the self-excited baroclinic waves.

c. Scaling magnitudes and parameter values

In the horizontal, the channel extends from 27.5° to 72.5°N, and thus we set the dimensional width at πL_y

---

[1] We will allow the nondimensional $\hat{x}$ to vary over $[0, 2\pi]$, while $\hat{y}$ varies only over $[0, \pi]$. This is motivated by the boundary conditions, which require no flow at the channel walls, and our choice of $\sin y$ as the gravest basis function in the meridional direction. [See sections 2b and 2e and Welch (1996).] Thus the dimensional length of the channel is given by $2\pi L_x$ and the dimensional width by πL_y; that is, δ is *twice* the ratio of channel width to length.

= 5000 km. We choose $\delta = 1.3$, which yields a dimensional width of $2\pi L_x = 7700$ km. Further discussion of these parameter values occurs in section 2e.

In the vertical, the model attempts to capture the bulk of the troposphere; hence the upper lid is placed at 200 mb (the approximate height of the midlatitude tropopause), the bottom at 1000 mb, and the depth of each layer is given by $\Delta p = 400$ mb (as in Stone 1978). Other parameter values are similar to those of Cehelsky and Tung (1991): $f_0 = 1 \times 10^{-4}$ s^{-1}, $\sigma_0 = 0.1$, $\beta = 0.2$, and $\nu = 0.008\,634\,8$ (a 6.7-day Ekman damping time). Finally $h'' = 0.001\,036\,175$, a 56-day Newtonian cooling time. This rather slow value was chosen to illustrate best the model equilibration; a sensitivity study of the model to h'' is included in section 6.

d. Radiative forcing and the Hadley solution

The model is forced by the radiative equilibrium zonal-mean temperature at the interface between the two layers. A simple calculation of radiative equilibrium appears in Lindzen (1990; see his Fig. 2.2), which shows that the forced temperature profile can be approximated by a simple cosine. We set $\overline{T}^{\dagger}_{\text{diml}}(y) = 0.5\Delta T^{\dagger} \cos y$ and vary the magnitude of the forcing by altering $\Delta T^{\dagger}$, a dimensional measure of the temperature difference across the channel. In our present climate, $\Delta T^{\dagger} \approx 80$ K [see Fig. 2.2 of Lindzen (1990)].

This radiative equilibrium temperature profile is translated into a forced streamfunction using the hydrostatic equation, $T \sim -\partial\Psi/\partial p$:

$$\Psi^{\dagger}_{1,\text{diml}}(y) = \frac{R\Delta p}{f_0 p_2}\frac{1}{2}\Delta T^{\dagger} \cos y \qquad (2.6)$$

$$\Psi^{\dagger}_{3,\text{diml}}(y) = 0. \qquad (2.7)$$

Ultimately the lower layer should be driven by momentum forcing from the Tropics (Tung and Rosenthal 1985, 1986), but here for simplicity we omit this feature by using rigid channel walls. Our model choices have ramifications on the resultant velocity profiles, which will be addressed in section 6.

Corresponding to this forcing there is a wave-free solution of (2.3)–(2.5), the so-called Hadley solution. This solution is used as an initial state in the nonlinear simulations.

e. Nonlinear solution method

To solve (2.3)–(2.5), a spectral tau method is used. The streamfunctions are expanded in eigenfunctions of the horizontal Laplace operator, with M and N modes retained in the zonal and meridional directions, respectively. (We call this an $M \times N$ model.) Using orthogonality, we obtain coupled ordinary differential equations for the coefficients. These equations are solved numerically using a Runge–Kutta method, with fast
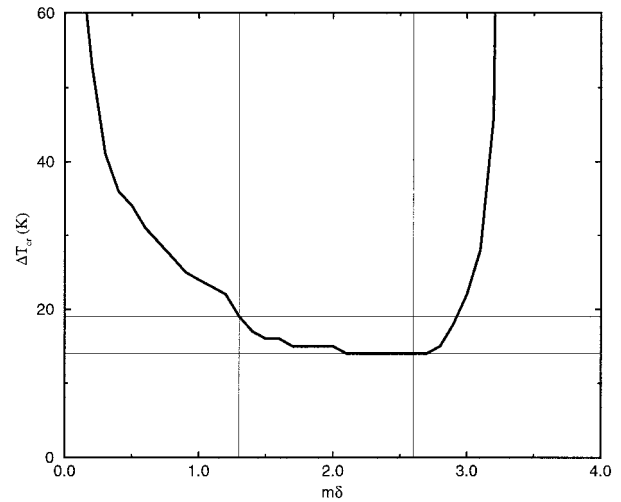

FIG. 1. Marginal stability curve (Im{mc_m} = 0; thick solid line) for the initial state. Thin vertical lines are at $m = 1$ and $m = 2$ for the geometry $\delta = 1.3$. Thin horizontal lines give the critical temperature gradients for $m = 1$ (upper line; $\Delta T_{\text{cr},m1} = 19$ K) and $m = 2$ (lower line; $\Delta T_{\text{cr},m2} = 14$ K).

Fourier transforms used for the nonlinear terms. For details of the solution method, see Welch (1996).

A ∇^4_{δ}-type subgrid damping term is added to the vorticity equation in each layer. This simulates the effect of the small scales, here truncated away, to which the enstrophy would otherwise cascade. The coefficient of subgrid damping, ν_s, is set as a function of the truncation level $M \times N$ so that only the eddy of smallest scale (the highest two wavenumbers retained in either direction) feels the effect of this numerical friction over that of real Ekman damping. To determine the smallest truncation that yields an accurate solution, the model was run at 10×10, 15×15, 21×21, 31×31, and 42×42 resolutions and the resulting equilibria compared. The resolution 21×21 was found to be the coarsest that had converged to the results of a model twice its size. Subsequently all simulations were run at 21×21 unless otherwise indicated.

The value of δ determines which wavelengths are permitted in the channel, that is, which will fit an integral number of times, as well as which of those wavelengths can be unstable. Figure 1 shows the marginal stability curve for perturbations to the initial Hadley state using $N = 21$. [Details of the linear stability analysis can be found in Welch (1996).] The value of δ determines how many waves are inside the unstable portion of the curve. For $\delta = 1.3$ the plot shows that at most two zonal waves can be linearly unstable for any $\Delta T^{\dagger}$, with the shorter wave (larger effective wavenumber $m\delta$) being the more unstable. This is the simplest possible nonlinear case, and thus we will use it to explore the baroclinic adjustment and wavenumber selection mechanisms. As mentioned in section 2c, $\delta = 1.3$ yields a channel of length 7700 km, which is approximately one-third of the circumference of the real

earth at 50°N. This choice is made to illuminate the nonlinear mechanism; a case with parameters yielding a realistic channel is addressed in a later work (Welch and Tung 1998).

Note that we retain many waves in both directions to yield a converged solution, but we choose parameter values such that only the first two of the many zonal waves can be unstable. Having only two zonal waves unstable does not mean that zonal waves 3–21 are not needed in the simulation. The small zonal scales, even though they are stable and have negligible amplitude and heat transport at equilibrium, do have a role in establishing that equilibrium: they are needed to represent properly the downscale enstrophy cascade that occurs in the real atmosphere. By retaining enough modes, and setting the magnitude of the subgrid damping coefficient ν_s appropriately, a small pathway is provided from the large scales, which gain energy from the forcing, to the small scales, which act as a slight damping force on larger modes. The alternative is truncating after wavenumber 2. However, such a severely truncated model can yield false equilibria and weather regimes, as pointed out by Cehelsky and Tung (1987). We must use a fine enough resolution to allow for a pathway of enstrophy to small scales, and we set the parameter values to yield only two modes unstable for a clear view of the dynamics.

3. The baroclinic adjustment mechanism

a. Basic features

In the nonlinear problem we are most interested in the equilibrium state to which the system evolves. Starting from the zonal mean state described in section 2d and perturbing each x and y mode with random but small amplitude, the system goes through a transient state and then settles into a dynamic equilibrium by approximately $t = 60$ days (not shown). To measure this equilibrium, values are averaged over the last 30 days (259 time steps) of a 231-day run (2000 time steps).

In particular, we are concerned with the zonal mean temperature at equilibrium. The model starts with the $\cos y$ profile of the imposed forcing. This shape exists more or less at equilibrium as well, but at a reduced magnitude (not shown). Thus a concise measure of the temperature profile, equilibrated or forced, is the difference or "gradient" across the channel, defined by

$$\Delta \overline{T} \equiv \overline{T}_2|_{y=0} - \overline{T}_2|_{y=\pi}. \quad (3.1)$$

We can approximate $\Delta \overline{T}$ with twice the magnitude of the temperature when projected onto $\cos y$ (Cehelsky and Tung 1991). This projection is easily available from our expansion of the streamfunctions mentioned in section 2e. This $\cos y$ approximation to $\Delta \overline{T}_{eq}$ is plotted with crosses in Fig. 2 for a wide range of forced gradients, $\Delta T^\dagger$. We see that the equilibrated temperature gradient rises slightly as the forcing is raised, but that it asymp-
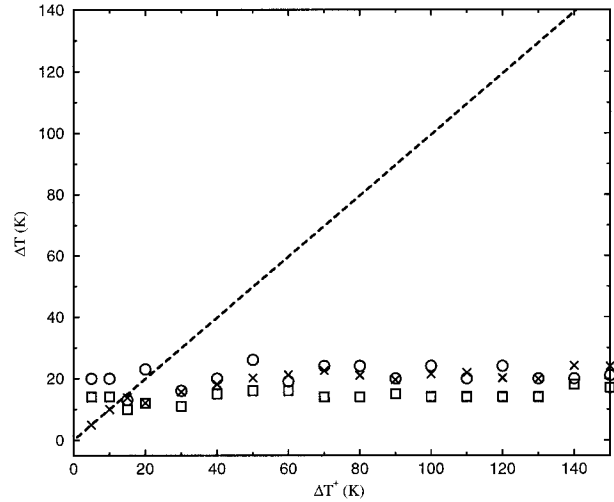

FIG. 2. Equilibrium temperature gradients (crosses) for a range of forcing for $\delta = 1.3$. Also shown is the Hadley solution (dashed line). Critical gradients from a linear stability analysis of the equilibrated flow at each forcing are given as circles (for $m1$) and squares ($m2$).

totes to a value that remains roughly constant even as the imposed temperature gradient varies by over 100%. This agrees with the observational results of Stone (1978) mentioned in the introduction. It must be that other components of the system are highly sensitive to the forcing, while the equilibrated temperature gradient is not.

We are also interested in the heat transport by each zonal mode at equilibrium. Consider the nondimensional thermodynamic energy equation (2.5), zonally averaged:

$$\frac{\partial \overline{T}_2}{\partial t} = -\delta \frac{\partial}{\partial y} \overline{(v_2' T_2')} + 2\sigma_0 \overline{\omega}_2 + 2h''(T^\dagger - \overline{T}_2), \quad (3.2)$$

where the hydrostatic equation $T \sim -\partial \Psi / \partial p$ has been used to express quantities in terms of the temperature at the interface of the two model layers (level 2). At equilibrium we have

$$\overline{T}_{eq} \equiv \overline{T}_{2,eq} \approx T^\dagger - \frac{\delta}{2\sigma_0} \frac{\partial}{\partial y} \overline{(v_2' T_2')} + \frac{\sigma_0}{h''} \overline{\omega}_2 \quad (3.3)$$

$$\approx T^\dagger + \frac{\sigma_0}{h''} \overline{\omega}_2^*, \quad (3.4)$$

where * indicates the transformed Eulerian mean residual circulation (TEM; Andrews et al. 1987):

$$\overline{\omega}_2^* \equiv \overline{\omega}_2 - \frac{\delta}{2h''} \frac{\partial}{\partial y} \overline{(v_2' T_2')}. \quad (3.5)$$

Evaluating (3.4) at the channel walls and subtracting, to yield "differential" values as in (3.1), yields

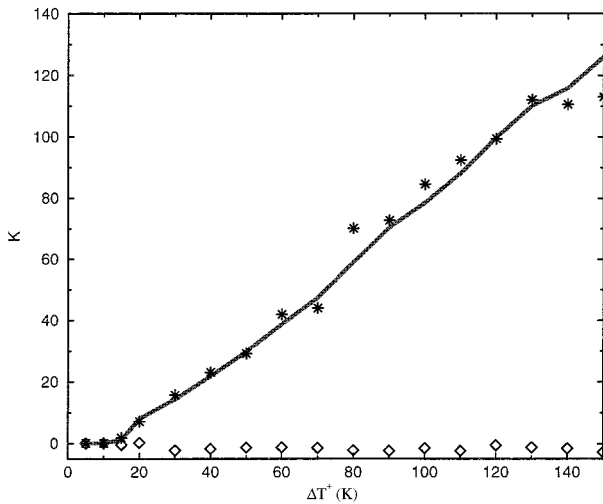$$\Delta \overline{T}_{eq} = \Delta T^\dagger + \frac{\sigma_0}{h''} \Delta \overline{\omega}_2^*, \quad (3.6)$$

FIG. 3. Measures of "flexibility" for $\delta = 1.3$: cross-channel gradient of residual mean vertical velocity, $\Delta T^\dagger - \Delta \overline{T}_{eq}$, at exact equilibrium (solid line); cross-channel gradient of residual mean vertical velocity, $-\sigma_0/h'' \Delta \overline{\omega}_2^*$, time-averaged in model equilibrium (asterisks); cross-channel gradient of Eulerian vertical velocity, $-\sigma_0/h'' \Delta \overline{\omega}_2$, time-averaged in model equilibrium (diamonds).

FIG. 4. Differential heat flux convergences, $\delta/2h'' \Delta \partial/\partial y (v_2' T'_2)$, at equilibrium vs forcing for $\delta = 1.3$. Solid line is for $m1$; dashed for $m2$; dot-dashed for $m3$.

which shows that it must be $\Delta \overline{\omega}_2^*$ that is the flexible component of the system if $\Delta \overline{T}_{eq}$ is robust as $\Delta T^\dagger$ changes. Figure 3 demonstrates this by plotting $\Delta T^\dagger - \Delta \overline{T}_{eq}$ versus forcing, showing the value $-\sigma_0/h'' \Delta \overline{\omega}_2^*$ would have at exact equilibrium, that is, if the time derivative in (3.2) were exactly zero. This differential residual mean vertical velocity rises approximately linearly with forcing. The actual model output, time-averaged and projected onto the cos$y$ component, is also shown in Fig. 3 as asterisks. These values fall approximately on the exact equilibrium line, corroborating that the residual mean vertical velocity is the flexible component of the system.

Is this flexibility due to the actual vertical motion or to differential heat flux convergence, that is, the first or the second term of (3.5)? To answer this question we have also plotted in Fig. 3 the cos$y$ projection of $-\sigma_0/h'' \Delta \overline{\omega}_2$. As these values are very small, it is seen that the Eulerian mean circulation has little effect on the cross-channel temperature gradient in this model: $\overline{\omega}_2$ is important near the channel boundaries, but overall the TEM vertical velocity is dominated by the eddy heat flux convergence.[2] Thus it is wave heat transport that is the single flexible component of the model. This also agrees with observations, which show eddy heat flux as

very sensitive to the forced temperature gradient (Stone and Miller 1980).

Now let us investigate the heat transport for individual waves. Figure 4 shows the differential heat flux convergence versus forcing for $m = 1$, 2, and 3 separately, again measured by twice the cos$y$ component. At low driving $m = 2$ transports most of the heat, whereas for medium and large drivings $m = 1$ dominates; $m = 3$ (and shorter waves) have a negligible contribution to the heat flux at all forcings. Here the model agrees with analytic and numerical studies and observations (see the introduction) in the selection of a wave longer than the least unstable wave as dominant.

The major results above have previously been documented by Cehelsky and Tung (1991). However, that work did not address *how* the dominant wave is selected and what will be the equilibrated temperature gradient, except at high drivings. These points will be explained here via a conceptual model for this case of $\delta = 1.3$.

b. A conceptual model

Figure 5 schematically displays what is expected for our nonlinear system of two unstable waves. For very low forcings, no waves will be unstable (as predicted by Fig. 1) and there will be no eddy heat transport. The equilibrated temperature gradient will simply adjust to the imposed gradient. This is the so-called Hadley regime, which we name Regime A, and it exists for $\Delta T^\dagger < \Delta \overline{T}_{cr,m2}$. Here $\Delta \overline{T}_{cr,m2}$ is the critical gradient for wavenumber 2 from a linear stability analysis of the zonal mean flow.

At slightly higher forcings, the Hadley state will be unstable to perturbations of zonal wavenumber 2, and hence the Hadley solution will not be selected by the

---

[2] The heat flux convergence and the vertical velocity can have very complicated meridional profiles at equilibrium. However, because $\overline{T}_2(y)$ retains roughly a cos$y$ shape, (3.3) shows that only the cos$y$ projection of the heat flux and the vertical velocity have any substantial effect on the temperature; their other projections must cancel each other. This demonstrates the usefulness of the transformed Eulerian mean.
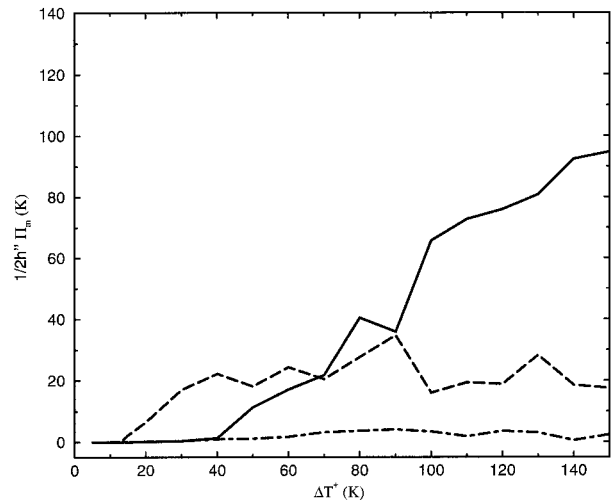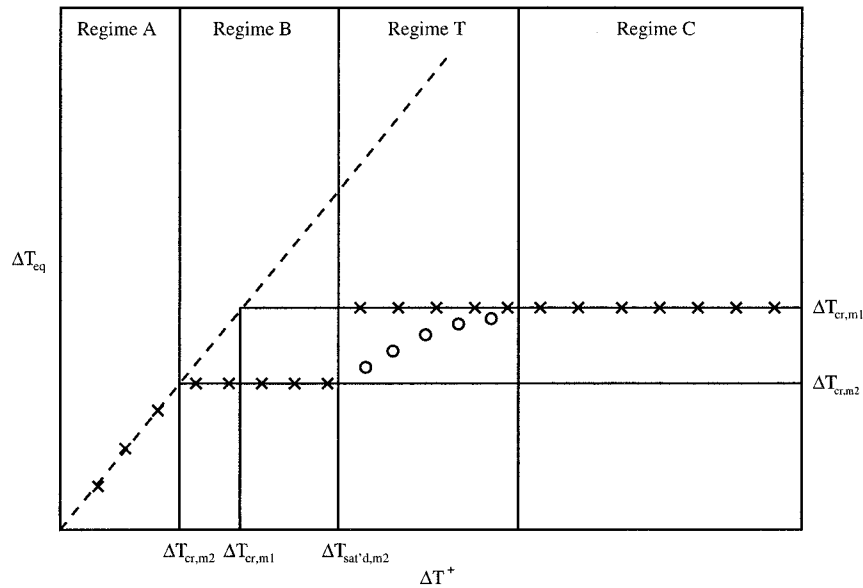
FIG. 5. Conceptual model of baroclinic adjustment for a geometry with two waves linearly unstable. Equilibrium temperature gradient indicated by crosses and, in Regime T, by circles; Hadley solution given by dashed line; solid horizontal lines indicate $\Delta \overline{T}_{cr}$ for $m1$ (upper) and $m2$ (lower); solid vertical lines are regime boundaries.

model atmosphere. Wavenumber 2 will grow and transport heat poleward, reducing the temperature gradient from its imposed value. For $\Delta T^{\dagger} < \Delta \overline{T}_{cr,m1}$, it is easy to reason what will occur: wavenumber 2 will grow and extract energy from the mean flow, thereby transporting heat and reducing the zonal mean temperature gradient, until the mean flow has been adjusted such that $m2$ is no longer unstable. Thus we expect $\Delta \overline{T}_{eq} \approx \Delta \overline{T}_{cr,m2}$ in this Regime B as long as wavenumber 1 is not unstable. This is the simple baroclinic adjustment process envisioned by Stone (1978).

The same argument can be made even for forcings slightly higher than $\Delta \overline{T}_{cr,m1}$. Because $m2$ will be more unstable than $m1$, it will still be expected to extract more energy from the mean flow and hence regulate the temperature gradient more than the longer wave. As $\Delta \overline{T}$ decreases, $m1$ will be stabilized first, allowing $m2$ to again reduce the temperature gradient down to *its* critical value. This is also encompassed by Stone's theory of (linear) baroclinic adjustment. Regime B, therefore, extends from $\Delta T^{\dagger} = \Delta \overline{T}_{cr,m2}$ up to *and beyond* $\Delta \overline{T}_{cr,m1}$. This regime is defined throughout by wavenumber 2 dominating the heat transport and by equilibration of the temperature gradient at the value of $\Delta \overline{T}_{cr,m2}$.

Should Regime B be expected to extend up to arbitrarily large forcings? As shown in Fig. 3, the total heat transport (equivalently, the differential residual mean vertical velocity) increases linearly with forcing in order to maintain a robust equilibrated temperature gradient. Thus for Regime B to extend indefinitely, the heat transport by $m2$ (alone) would have to increase linearly with the forcing. However, as heat flux convergence rises, so do the wave streamfunction amplitude, the wave potential vorticity (PV), and the meridional gradient of wave PV. Following the reasoning of Garcia (1991), we expect a mode to break when its wavy PV gradient is larger than the zonal mean PV gradient. Thus arbitrarily high heat transport by wavenumber 2 is unlikely. Furthermore, since PV increases with wavenumber more quickly than heat transport does, $m1$ could transport the same amount of heat as $m2$ while creating a smaller wavy PV gradient. Thus it seems possible that wavenumber 1 would be able to transport heat in forcing regimes where wavenumber 2 could not. (See section 4a for further discussion.)

Given the above argument, it must be that wavenumber 2 encounters some threshold value of heat transport. Should the total heat required by the system (in order to achieve a robust temperature gradient) exceed this value, the shorter wave will be unable to transport the total heat, and other zonal modes must come into play. Thus Fig. 5 shows that Regime B will exist only for $\Delta \overline{T}_{cr,m2} < \Delta T^{\dagger} < \Delta \overline{T}_{sat'd,m2}$, where "sat'd" signifies the threshold level where wavenumber 2 reaches saturation. Note that the upper limit of Regime B is determined, not by the critical temperature gradient for wavenumber 1 but by the heat flux threshold for wavenumber 2. That is, the boundary between Regime B and Regime T, defined below, marks the shift from a (quasi) linear to a nonlinear regime.

As the forcing is raised above $\Delta \overline{T}_{sat'd,m2}$ and the total heat requirement continues to increase, other zonal waves must play a more important role. Wavenumber 1 is expected to be the additional heat transporter because it has a smaller wavenumber than $m2$ and thus should be less likely to break, as argued above. The next
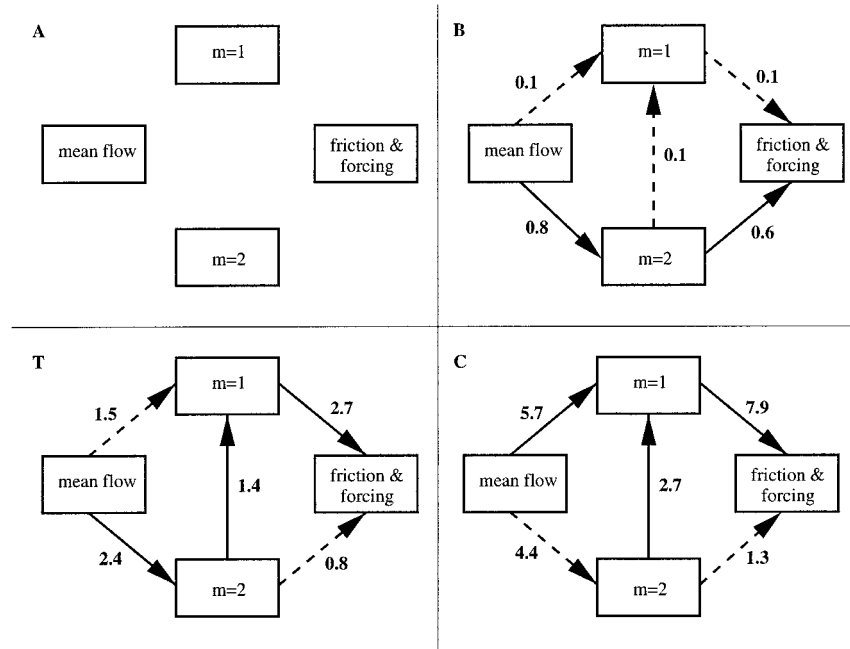
FIG. 6. Schematics diagrams of energy flow for nonlinear equilibria at different forcings: Regime A (panel A); $\delta = 1.3$, $\Delta T^\dagger = 25$ K (panel B); $\Delta T^\dagger = 50$ K (panel T); and $\Delta T^\dagger = 90$ K (panel C). Solid arrows indicate heavy energy transfer, while dashed arrows indicate weaker transfer. Numbers next to arrows are rate of change of energy, in 1×10^{-5} nondimensional units. The net energy flow into any mode in a panel may not be exactly zero, because there is a small nonlinear transfer to shorter waves and to the mean flow that is not shown, and because the total growth rate may not be precisely zero in our time average. In addition, there is some difficulty in assigning nonlinear transfer *between* two specific modes, but since $m1$ and $m2$ are so much larger than all other modes in our cases of interest, this arbitrariness is small.

regimes are characterized by the fact that it is $m1$ that provides the flexible component to the system, transporting whatever additional heat is necessary beyond $m2$'s (constant) saturated contribution.

Figure 5 shows that $\Delta \overline{T}_{eq}$ shifts to a new, higher value for $\Delta T^\dagger > \Delta \overline{T}_{sat'd,m2}$. This is because, as the new flexible heat transporter, wavenumber 1 will determine the equilibrated temperature gradient: $m1$ will decrease $\Delta \overline{T}$ until $m1$ is no longer unstable so that $\Delta \overline{T}_{eq} \approx \Delta \overline{T}_{cr,m1}$ at these higher forcings. Note that this is *critical* equilibration, for the final state is critical relative to the mode dominating the heat transport.

The crosses of Fig. 5 show an abrupt jump in the equilibrium temperature gradient at the upper boundary of Regime B. This is not really to be expected, as Π_1 (the heat transport by zonal wave 1) will not truly dominate and determine the equilibrated temperature gradient until it grows larger than Π_2. We expect some sort of transition region after Regime B in which $\Delta \overline{T}_{eq}$ gradually rises from $\Delta \overline{T}_{cr,m2}$ to $\Delta \overline{T}_{cr,m1}$ as the forcing is increased and the total heat required to equilibrate the system increases. This transition regime (Regime T) is indicated in Fig. 5 with circles instead of crosses, and within it $m1$ plays the flexible role in the heat transport, but $\Pi_1 < \Pi_2$. Beyond this is Regime C, defined by $\Delta \overline{T}_{eq}$

$= \Delta \overline{T}_{cr,m1}$, which occurs only for the highest drivings when $\Pi_1 > \Pi_2$.

The above conceptual model can be summarized by a series of energy diagrams, one for each regime, as shown in Fig. 6. In each panel, the movement of energy from the zonal mean flow to the waves, between the waves, and to damping (Ekman, subgrid, and thermal) is indicated by arrows. Solid arrows represent the primary energy flux and dashed arrows the lesser flux. (The numbers can be neglected for now; they will be discussed in section 5.) Regime A is simple: as no modes are unstable, there is no extraction of energy from the mean flow and hence no energy in any wave. In Regime B, $m2$ extracts energy quasi-linearly from the mean flow (i.e., transports heat) and loses its energy to viscous and thermal damping. The longer wave can also extract energy from the mean flow, and there can be a small nonlinear transfer between $m1$ and $m2$, but the dominant process is $m2$'s quasi-linear energy extraction and linear dissipative loss.

Regime C is the opposite of Regime B: the dominant process is $m1$'s quasi-linear energy extraction and linear dissipation; $m2$ can also extract and lose energy, but to a smaller degree. In Regime C there is an additional possibility of fairly large nonlinear transfer of energy

from $m2$ to $m1$, a manifestation of the saturation of wavenumber 2. This nonlinear transfer will be discussed in sections 4b and 5.

Regime T has an intermediate energy diagram: $m2$ still extracts more energy quasi-linearly from the mean flow than does $m1$, but it has reached its saturation level and hence transfers a large amount of its energy nonlinearly to $m1$. This longer wave experiences larger dissipation than $m2$, and thus the predominant energy pathway is energy gain by $m2$ and energy loss by $m1$, clearly a nonlinear pathway as it involves *both* waves. Note that this is the only regime in which the major energy pathway involves both waves.

For all forcings in this conceptual model, $m2$ will always be the most unstable wave at equilibrium, indicated by the fact that $\Delta \overline{T}_{cr,m2} < \Delta \overline{T}_{cr,m1}$ at all forcings in Fig. 5. One might expect it to dominate the energy extraction from the mean flow in all regimes. That is, one might expect the energy diagram for the transition regime to hold true for arbitrarily large forcings as well, in place of Regime C's scheme. This is not found in model runs, however (see below). Wavenumber 1 "takes over" from the shorter mode, rendering the equilibrium state at high forcing more quasi-linear as opposed to the clearly nonlinear equilibrium of Regime T. This is one of the surprises of the nonlinear baroclinic adjustment mechanism and will be elaborated in section 5.

Note that the baroclinic adjustment mechanism has been defined here for *all* levels of forcing. We now corroborate this conceptual mechanism with output from the two-layer model.

c. Model output

Returning to Figs. 2 and 4, we can identify each of the regimes of the conceptual model with the numerical output. Regime A is easily seen to occur for $0 < \Delta T^{\dagger} \leq 13$ K; at these low forcings, there is no heat flux by any mode and the equilibrated temperature gradient agrees with the Hadley solution. Note that the upper cutoff of Regime A in the nonlinear simulation (13 K) agrees with the critical gradient for the most unstable wave as determined from linear stability analysis (14 K from Fig. 1).

Regime B can be identified from Fig. 4 as the region outside the Hadley regime in which there is no appreciable heat flux by wave 1. This occurs for $13 \leq \Delta T^{\dagger} \leq 40$ K. Figure 2 shows that in this forcing range the temperature gradient equilibrates approximately at the critical gradient for mode 2. Note that this range extends well above the forcing at which $m1$ becomes unstable, that is, 19 K from linear stability analysis (Fig. 1). Also, $m2$ is clearly the flexible component of the system in Regime B, for its heat transport grows approximately linearly with forcing in this range in Fig. 4.

Regime C, in which $\Pi_1 > \Pi_2$, is discernible from Fig. 4 as $\Delta T^{\dagger} \geq 70$ K. This is corroborated by Fig. 2, which shows that in this range $\Delta \overline{T}_{eq} \approx \Delta \overline{T}_{cr,m1}$.

Regime T is the range between B and C: $40 \leq \Delta T^{\dagger} \leq 70$ K. We notice that in this range the equilibrated temperature gradient grows from approximately $\Delta \overline{T}_{cr,m2}$ to $\Delta \overline{T}_{cr,m1}$ as the forcing is raised, corresponding to the circles of Fig. 5.

From the dividing line between Regimes B and T, we can see that $m2$'s heat transport threshold is $\Delta \overline{T}_{sat'd,m2} \approx 40$ K. For all higher forcings, $m2$ is saturated and thus its heat transport remains roughly constant, as Fig. 4 more or less shows. Correspondingly, as the forcing increases from $\Delta T^{\dagger} = 40$ K, the wavenumber 1 heat transport grows approximately linearly with forcing, as it has assumed the flexible role in the system.

Our conceptual model of Fig. 5 has been shown to work for forcings from $\Delta T^{\dagger} = 5$ to 150 K. This is a wide range, given that our current climate has a solar driving of $\Delta T^{\dagger} \approx 80$ K.

We reiterate that the temperature gradients in Regimes B and C exhibit *critical* equilibration, where we define critical relative to the dominant heat transporting mode in the modified flow. Relative to the most unstable mode, however, Regime C equilibria appear to be supercritical throughout! (See Fig. 2.) This explains the discrepancy between our critical equilibration and the "supercritical equilibration" of geostrophic turbulence studies (Salmon 1980; Vallis 1988); it is simply a semantic difference. Salmon, in fact, included a calculation in his work that demonstrates critical equilibration. First he determined the wave at equilibrium that has the maximum extraction of energy from the mean flow, that is, the maximum $F(k)$ (his notation) or northward heat transport. Simultaneously, he calculated at what wavenumber the equilibrated zonal-mean flow would be critical [see Table III in Salmon (1980)]. For both cases that he investigated, the wavenumber at which the equilibrated flow is critical turns out to be the same as the wavenumber of maximum heat transport. This is the very essence of the baroclinic adjustment mechanism.

In another corroboration of critical equilibration, Cai (1992) found that his analytic quasi-linear model (see the introduction) showed neutralization of the mean flow by two different methods: reduction of the mean baroclinicity and meridional modification of the mean flow that "reduces the instability so that the equilibrated zonal flow is neutral even though the mean value of it is supercritical" (Cai 1992, 1600). Here we analyze the stability of the full equilibrated flow, including its detailed meridional profile; we do not simply use the initial cosy shape with the cross-channel gradient adjusted to $\Delta \overline{T}_{eq}$. If Cai's analysis had been performed as ours here, his model's equilibration would have been termed critical. In addition, Cai points out the importance of calculating stability relative to the dominant heat transporting mode: "the adjusted zonal flow is indeed neutral with respect to the wave . . . itself" (Cai 1992, 1600).

Heretofore we have termed the equilibrium "robust," but we have substantiated this claim only by showing that the equilibrated temperature gradient does not

change much with forcing. In fact, there are several quantities that are insensitive to the level of forcing: the zonal mean potential vorticity, the zonal mean meridional gradient of PV, and the zonal mean potential enstrophy, each separately in each layer of the fluid. To demonstrate this, begin with the definition of (nondimensional) PV in each layer:

$$Q_j \equiv 1 + \beta\left(y - \frac{\pi}{2}\right) + \nabla_\delta^2 \Psi_j + \frac{j-2}{2\sigma_0}(\Psi_1 - \Psi_3),$$
$$j = 1, 3, \qquad (3.7)$$

where the "1" is a nondimensionalized f_0. The equilibrated zonal average can be approximated:

$$\overline{Q}_j \approx 1 + \beta\left(y - \frac{\pi}{2}\right) + \gamma_j \overline{T}_{2,\mathrm{dim'1}}(y), \qquad j = 1, 3,$$
$$(3.8)$$

where the relative vorticity has been neglected because model output shows it to be small at equilibrium.[3] The γ_j are nondimensionalizing constants that can be determined from (2.6)–(2.7); note that $\gamma_1 < 0$. As discussed earlier, the temperature profile retains a cos$y$ shape and has a robust magnitude at equilibrium. Thus (3.8) shows that $\overline{Q}$ in each level will be similarly insensitive to the forcing. This immediately implies as well that the zonal mean enstrophy, $\overline{Q}_j^2$, $j = 1, 3$, will be robust.

The zonal-mean meridional PV gradient in each layer is, from (3.8),

$$\frac{\partial \overline{Q}_j}{\partial y} \approx \beta + \gamma_j\left(\frac{\partial \overline{T}_2}{\partial y}\right)_{\mathrm{dim'1}}, \qquad j = 1, 3. \quad (3.9)$$

Again, because the temperature profile at equilibrium is robust, so must be its meridional gradient and the PV gradient in each layer. In particular, if we assume that the temperature distribution at equilibrium can be approximated by $\overline{T}_{2,\mathrm{eq,dim'1}} \approx 0.5(\Delta \overline{T}_{\mathrm{eq}})_{\mathrm{dim'1}} \cos y$, we can estimate the average zonal mean PV gradient over the channel:

$$\langle \overline{Q}_{j,y} \rangle \approx \beta + \hat{\gamma}_j \Delta T_{\mathrm{eq}}, \qquad (3.10)$$

where

$$\hat{\gamma}_j \equiv -0.5\frac{2}{\pi}\gamma_j = (2 - j)\frac{1}{\pi}\frac{1}{2\sigma_0}\frac{\Delta pR}{p_2 L_y^2 f_0^2}, \qquad j = 1, 3.$$
$$(3.11)$$

Here angle brackets indicate a meridional average. This approximation for the zonal mean PV gradient can be used in the next section to determine wave saturation levels.

---

[3] Note that y here is nondimensional even though $\overline{T}_2$ is dimensional.

4. The wavenumber selection process

In our conceptual model we reasoned for the existence of a threshold of heat transport for wavenumber 2. We now develop a method to quantify the argument. Following this in section 4b, we describe the impact of such a threshold on the evolution of the system toward equilibrium.

a. Derivation of a heat transport threshold

The magnitude of the wavy PV gradient for a specific mode can be determined from the size of its heat flux convergence. First, let us calculate the magnitude of the heat transport as a function of streamfunction amplitudes. The zonal mean heat flux convergence by zonal mode m is given by

$$\Pi_m = -\delta\frac{\partial}{\partial y}\overline{(v_2' T_2')} = \delta\frac{\partial}{\partial y}\overline{(\Psi_{1,x}' \Psi_3')}. \quad (4.1)$$

The average magnitude of this heat flux can be approximated as

$$\langle|\Pi_m|\rangle \approx \delta m\frac{1}{2}|\Psi_1'||\Psi_3'|\sin\phi_m \approx \delta m\frac{1}{2}|\Psi_1'|^2 \sin\phi_m. \quad (4.2)$$

Here $\phi_m = \langle \arg\Psi_{1,m}' - \arg\Psi_{3,m}'\rangle$, the average vertical phase tilt of the wavenumber m component of the streamfunction.

Similarly, we can approximate the magnitude of the wave PV gradient from the upper streamfunction amplitude. The meridional gradient of the upper-layer wavy PV is, from (3.7),

$$Q_{1,y}' = \frac{\partial}{\partial y}\left[\nabla_\delta^2 \Psi_1' - \frac{1}{2\sigma_0}(\Psi_1' - \Psi_3')\right] \approx \frac{\partial}{\partial y}\nabla_\delta^2 \Psi_1',$$
$$j = 1, 3, \qquad (4.3)$$

where the approximation has been confirmed with model output. This gives

$$\langle|Q_{1,y}'|_m\rangle \approx \delta^2 m^2|\Psi_1'|. \quad (4.4)$$

Combining (4.2) and (4.4) yields

$$\langle|Q_{1,y}'|_m\rangle \approx \sqrt{\frac{2\delta^3 m^3}{|\sin\phi_m|}}\sqrt{\langle|\Pi_m|\rangle}. \quad (4.5)$$

Therefore the magnitude of the wavy PV gradient corresponding to a certain heat flux can be inferred for a given zonal mode. Notice from (4.5) that shorter waves (larger m) correspond to higher wavy PV gradients, all other things being equal (e.g., the phase tilt, which we have found only to enhance the above effect). Specifically, $m2$ transporting a certain amount of heat will yield a larger wavy PV gradient, by at least a factor of $(2^3)^{1/2} \approx 3$, than the same amount of heat transport by $m1$. We will use this fact below.

Garcia (1991) proposed that a large wavy PV gradient will lead to breaking if it exceeds the zonal mean PV

gradient. This is simply a generalization of the Charney–Stern theorem (Charney and Stern 1962), where the background flow now is the zonal mean flow plus a long-scale wave ($m = 1$ or 2 in our case). Perturbations of much smaller scales will see this background flow as zonally constant. Through a separation of scales, therefore, we can argue that if the *total* PV gradient $Q_y = \overline{Q}_y + Q'_{y,m}$ has negative as well as positive regions, then the flow is unstable to secondary perturbations. This is possible if the wavy PV gradient exceeds the zonal mean gradient in magnitude: $|Q'_{y,m}| > \overline{Q}_y$ for some y.

As discussed in section 3c, the zonal-mean PV gradient in either layer is a robust feature of equilibrium; it remains roughly constant as the forcing is raised. In contrast, the heat flux required to achieve baroclinic adjustment rises linearly with the forcing; Fig. 3 shows that it is approximately the difference between the imposed temperature gradient and the known (robust) equilibrated temperature gradient. Therefore, for $m2$ to transport all the heat required at equilibrium, we see from (4.5) that its corresponding PV gradient must rise with the driving. Thus, we expect the wavy PV gradient corresponding to wavenumber 2 to exceed the constant zonal mean value $\overline{Q}_y$ at some forcing. At this threshold, the shorter wave will break and saturate. Furthermore, (4.5) shows that the PV gradient for $m1$ will rise more slowly with heat transport than the PV gradient for $m2$. Thus wavenumber 1 will have a higher saturation level than wavenumber 2's threshold; wavenumber 2 will break before wavenumber 1 does. We have tested the above theory on the current case of $\delta = 1.3$, and it yields approximately the same saturation level for $m2$ as is observed in the nonlinear simulations.

Note that this method is based only on robust features of the equilibrium, primarily the equilibrated temperature gradient. Once the dominant wave is determined, we can estimate the equilibrated temperature gradient as the critical gradient of the modified flow relative to this dominant wave. It turns out, however, that the critical gradients of the *equilibrated* flow are similar to those of the initial (Hadley) state. Figure 1 gives the critical temperature gradient for $m1$ in the Hadley flow as approximately 19 K; in Fig. 2 at equilibrium the value is 21 K on average in Regime C. From the same figures, $m2$'s critical gradient in the Hadley state is approximately 14 K, with an equilibrated value of 12 K on average in Regime B. Thus, using only the initial (Hadley) flow, and robust measures of the equilibrium, one should be able to determine a priori which wave will dominate the heat transport at equilibrium and what will be the approximate temperature gradient for a wide range of forcings.

b. Wave breaking

In a system at high driving, exactly how does $m1$ grow to dominate over $m2$ as a function of time? The selection of a longer, less unstable wave in a multiwave

system has been documented *at equilibrium* by other authors (see the introduction). However, the *evolution* of such a system to equilibrium is rarely described.

We consider the case $\delta = 1.3$ and $\Delta T^\dagger = 50$ K, which falls into Regime T. This forcing has been selected because it is large enough for wave saturation to occur, yet small enough that the process evolves slowly so as to be discernible. Because it is in the transition regime, this case has the additional interest of being slightly more complicated than others, a point that we will discuss later in this section. Results from other forcings within Regime T are qualitatively similar to that considered here. Evolution to equilibrium in Regime C shows the same major features as in the case here and will not be shown.

The evolution depends on the particular initial conditions chosen, but simulations from various initial conditions of our two-layer model demonstrate that *regardless* of the initial state, the equilibrium state is similar for the same forcing. Thus our model is robust in another sense: it does not display the hysteresis observed by other authors, for example, Chou (1995), and any initial state can be chosen. We start from the (perturbed) Hadley state, which is unstable to both wavenumber 1 and 2 disturbances.

Beginning with the zonal mean state, the evolution to equilibrium can be divided into three phases. In the first phase, $t = 0$–7 days, zonal wavenumber 2 grows most quickly because it is the most unstable wave. This is shown for $t = 0$ in Fig. 1, but it also holds true at later times (not shown). The nature of the instability at $t = 0$ can be derived from (2.6)–(2.7). Differentiating with respect to y yields $U \sim \sin y$, and hence $\beta - \overline{U}_{yy} \sim \beta + \sin y$, which is positive throughout the channel. By the Charney–Stern theorem (Charney and Stern 1962), this flow is barotropically stable. Thus the initial growth is due to baroclinic instability only but is modified by barotropic shear.

Wavenumber 1 also grows during this phase I, because the Hadley state at $\Delta T^\dagger = 50$ K is highly unstable to perturbations of that wavelength. However, $m1$ grows at a lesser rate than $m2$ because the flow is less unstable to the former (Fig. 1). Both waves grow by extracting energy from the mean flow. Nonlinearities play a minor role at this early stage.

Phase I appears to be the simple baroclinic adjustment mechanism: the most unstable wave grows in amplitude, transporting heat and decreasing the overall temperature gradient, thereby reducing its own instability (not shown). Unlike the theory proposed by Stone (1978), however, wavenumber 2 cannot reduce the temperature gradient to its critical level. Instead, $m2$ reaches its threshold of heat transport and nonlinear dynamics take over in phase II of the evolution.

To describe the behavior in phase II, we will use contour maps over time of potential vorticity at level 1, that is, Q_1 from (3.7). These are shown in Fig. 7 for the first part of phase II. Here Q_1 is an approximation to
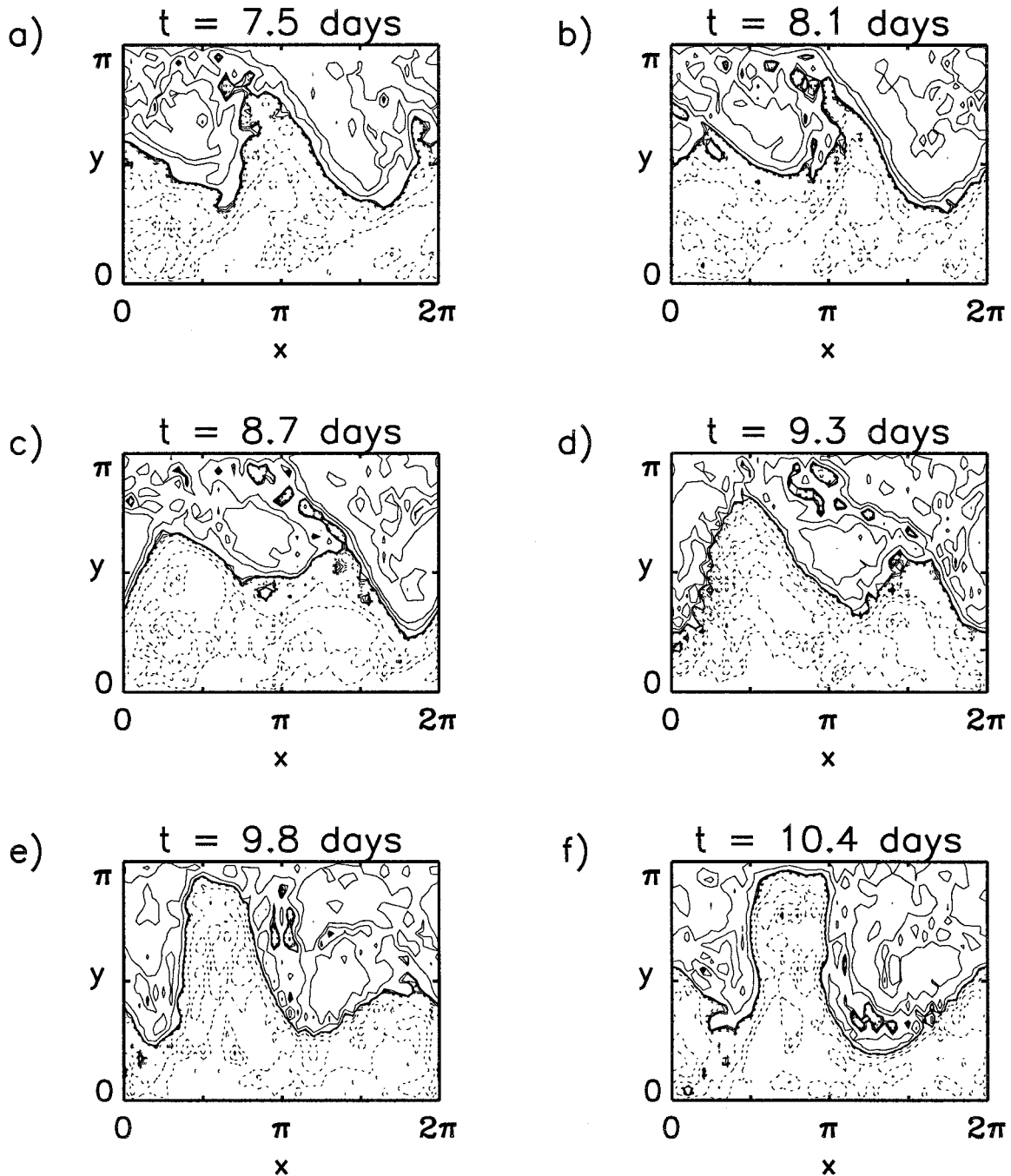
FIG. 7. Contour maps over time of potential vorticity in the upper layer vs x and y for phase II of the case $\delta = 1.3$, $\Delta T^{\dagger} = 50$ K. Thick solid line is the nondimensionalized f_0-contour; thin solid and broken lines indicate $Q_1 > f_0$ and $Q_1 < f_0$, respectively. (Contour interval is not constant.)

isentropic potential vorticity in the upper troposphere. At $t = 7.5$ days, zonal wavenumber 2 is evident in Fig. 7a (by counting the number of ridges or troughs in the dark PV contours) due to its dominant quasi-linear growth during phase I. At this early time, with only moderate wave amplitudes and curvatures, the meridi-

onal gradients of total potential vorticity are still dominated by β [see (3.7)] and hence mostly positive. As time progresses, the wave attempts to grow further because it is still unstable. However, the opposite potential vorticities in the northern and southern parts of the channel in Fig. 7a work against each other, twisting up the
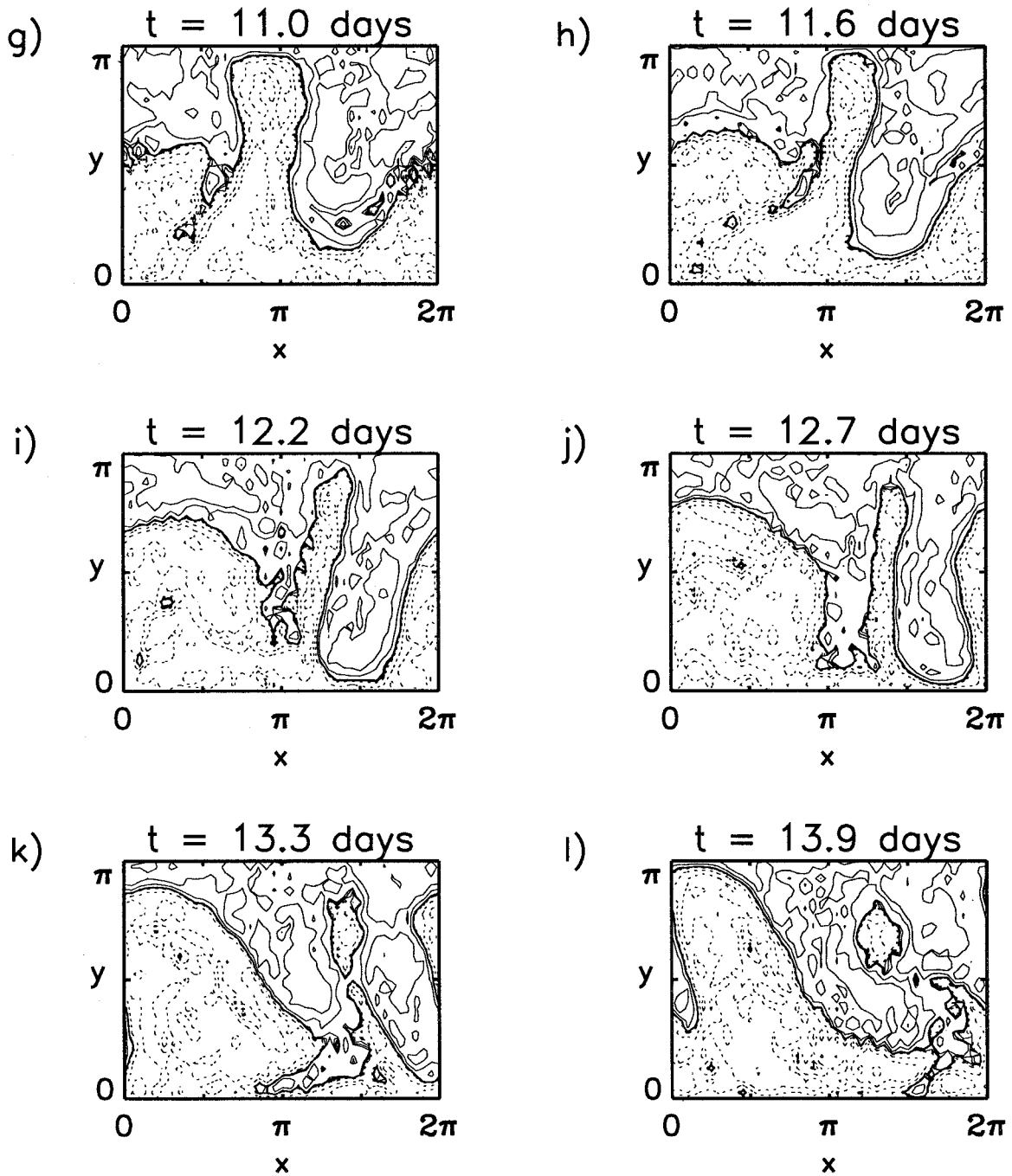
g) t = 11.0 days

h) t = 11.6 days

i) t = 12.2 days

j) t = 12.7 days

k) t = 13.3 days

l) t = 13.9 days

Fig. 7. (*Continued*).

contours and (by conservation of potential vorticity[4]) creating long thin tongues of PV as seen in Fig. 7b and later in Fig. 7h. This causes regions of negative total

meridional potential vorticity gradient, Q_y, as expected from our discussion in the previous section. When a long tongue is stretched out, as in Figs. 7b or 7h, small-scale instabilities arise on the sides of the tongue (Figs. 7b,i) and begin to pinch off the tongue (Figs. 7c,j), breaking it into blobs (Figs. 7d,k). These blobs, in turn, cause new regions of negative PV gradient and thus are broken up to even smaller sizes (Figs. 7e–f,l). This continues on and on until the blobs become of small enough

[4] We note that potential vorticity in our case is not materially conserved in that there is friction and forcing in the dynamics. However, the twisting up and stretching of PV contours obviously still occurs in Fig. 7 and thus the argument is relevant here.
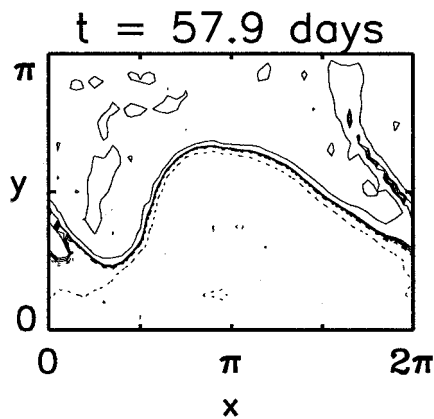
FIG. 8. As in Fig. 7 but for $t = 58$ days in phase III.

scale that viscous effects are significant, at which point they are dissipated completely.

Note that we can now confirm the separation of scales argument used here and in section 4a. The scales of the largest blobs, as in Fig. 7l, are of wavenumber $m \approx 7$, which is much smaller than the $m = 2$ wave on which they act.

The dynamics documented here follow the pattern of planetary "wave breaking" in the stratosphere as shown by McIntyre and Palmer (1983, 1984). When wave amplitudes are large enough, a rapid and irreversible deformation of material contours occurs. By the stretching, secondary instability, and dissipation mechanisms discussed above, waves break and deposit their PV into the region surrounding the sharpest contour gradients. This region, known as the surf zone, experiences significant mixing due to the wave breaking, and thus it becomes somewhat homogenized with only weak gradients of potential vorticity. In our case, zonal wavenumber 2 grows to a certain amplitude and then breaks, yielding regions of more uniform Q_1 on either side of the sharp potential vorticity gradient. This is evident in contour maps in phase III, after wave 2 has broken; an example is shown in Fig. 8 for $t = 58$ days.

In causing a redistribution of potential vorticity, wave breaking is an efficient way for transient eddies to affect the time-mean flow. The process is inherently nonlinear (as the requirement of contour deformation above implies), and thus in phase II there is a large nonlinear transfer of energy out of $m2$. Quasi-linear growth of $m2$ continues in this phase, as wavenumber 2 is still unstable, but the growth cannot overcome the nonlinear drain. In this way, the shorter wave is said to be "nonlinearly saturated." This agrees with Whitaker and Barcilon's (1995) demonstration that large nonlinear transfer out of the most unstable wave is what prevents it from dominating at equilibrium.

While wavenumber 2 is saturating, wavenumber 1 continues to extract energy from the mean flow, for it is still linearly unstable. Unlike wavenumber 2, it does not break and saturate, but rather receives most of the energy transferred nonlinearly out of $m2$. Thus during this phase wavenumber 1 grows through both wave–mean flow interaction and nonlinear transfer, while wavenumber 2 grows quasi-linearly but decays nonlinearly.

The end of phase II is at $t \approx 24$ days; by then wavenumber 1 has emerged as the most energetic wave due to the saturation of wavenumber 2. This can already be seen at $t = 13.9$ days in Fig. 7l: compare this panel, where the overall shape is that of wavenumber 1, with Fig. 7a, where wavenumber 2 is clearly dominant. This becomes more obvious as $t \rightarrow 24$ days (not shown), for then the breaking of wavenumber 2 is almost completely overshadowed by the large amplitude of wavenumber 1. It is very clear at $t = 58$ days in Fig. 8. Note that the breaking of $m2$ continues to and throughout equilibrium, but it is dominated by the larger quasi-linear dynamics of $m1$.

For $t > 24$ days, the magnitudes and energetics of the different zonal modes have been established and an equilibrium must only be maintained. This is phase III. At forcing levels in Regime B and C this maintenance is clear: the dominant wave simply equilibrates the temperature gradient at its critical value. In the transition regime, however, the competition between modes is ongoing, and hence the equilibrium is more complicated. Each wave attempts to reduce the temperature gradient down to its $\Delta \overline{T}_{cr}$, but both have limitations on their ability to "control" the dynamics: wavenumber 2's heat transport is capped at its threshold value, and wavenumber 1 is transporting less heat than $m2$. Thus neither wave clearly dominates and the temperature gradient equilibrates at a value intermediate to the two critical gradients (Fig. 2). Panel T of Fig. 6 shows the energetics in phase III for this forcing of $\Delta T^\dagger = 50$ K, now with actual numbers. (Section 5 explains how these were calculated.) Wavenumber 1 is sustained in part by quasi-linear energy extraction from the mean flow and in part by nonlinear transfer from wavenumber 2. Wave $m2$, on the other hand, is maintained by a balance between quasi-linear growth and nonlinear saturation.

There is an interesting paradox in the transition regime: while wavenumber 2 dominates the heat transport at equilibrium (Fig. 4), wavenumber 1 has the most energy (Fig. 8). This is not inconsistent, for the two measures are qualitatively different: heat transport is a rate of change of energy and is distinct from energy itself. This "dual dominance" is more evidence of the complicated nature of Regime T and why it equilibrates at a noncritical temperature gradient.

5. Nonlinearities

In this section we point out exactly how nonlinearities are part of the baroclinic adjustment mechanism. Cehelsky and Tung (1991) showed that for high forcing, while the selection of the dominant wavenumber is an inherently nonlinear phenomenon, the maintenance of the

equilibrium is essentially quasi-linear. Here we extend these ideas to all the regimes of Fig. 5.

The schematic energy diagrams of Fig. 6 will be used, now confirmed with actual data. Following Whitaker and Barcilon (1995), we calculated the nondimensional perturbation energy E' at equilibrium, where "perturbation" signifies deviation from the time and zonal mean:

$$E' = \frac{1}{2}\left[\delta^2\left(\frac{\partial\Psi_1'}{\partial x}\right)^2 + \left(\frac{\partial\Psi_1'}{\partial y}\right)^2 + \delta^2\left(\frac{\partial\Psi_3'}{\partial x}\right)^2 \right.$$
$$\left. + \left(\frac{\partial\Psi_3'}{\partial y}\right)^2 + \frac{1}{2\sigma_0}(\Psi_1' - \Psi_3')^2\right]. \quad (5.1)$$

This energy was horizontally averaged and separated by zonal wavenumber. Also calculated were the rate of each wave's energy growth or decay, derived by forming (2.3)–(2.5) into an energy equation. The energy gained and lost by each wave was split into parts: that due to extraction from the mean flow (i.e., wave–mean flow interaction), that due to nonlinear transfer from or to other wavenumbers (wave–wave interaction), and that due to dissipation, Newtonian forcing, and subgrid damping (linear processes). Numbers next to the arrows in Fig. 6 represent the time-averaged values of these (nondimensional) energy growth rates at equilibrium for three cases: $\Delta T^\dagger = 25$ K (panel B), $\Delta T^\dagger = 50$ K (panel T), and $\Delta T^\dagger = 90$ K (panel C).

For $\Delta T^\dagger = 25$ K (Regime B) the numbers confirm that the dynamics for low forcings (but outside the Hadley regime) are the simple baroclinic adjustment envisioned by Stone (1978). Nonlinearities are unimportant.

For the transition regime, we argued in the previous section that for $\Delta T^\dagger = 50$ K nonlinearities are necessary in maintaining equilibrium. This is corroborated by the numbers for panel T (Fig. 6) and is true at all such intermediate forcings.

We expect nonlinearities to be similarly important for Regime C. This is apparent from Fig. 2, which shows the critical temperature gradients for wavenumbers 1 and 2. Because $\Delta\overline{T}_{\mathrm{cr},m2} < \Delta\overline{T}_{\mathrm{cr},m1}$ throughout this regime, $m2$ is more unstable than $m1$ even at equilibrium! (We will return to this point later in this section.) Obviously nonlinear processes must be involved in maintaining the equilibria, otherwise $m2$ as the more unstable wave would certainly dominate.

Panel C (Fig. 6) shows results for $\Delta T^\dagger = 90$ K in Regime C. The energetics are as described in the conceptual model: wavenumber 1 has the largest extraction from the mean flow (equivalently, the largest heat transport) and nonlinear transfer from the shorter to the longer mode occurs at equilibrium. The wave-mean extraction by the shorter wave does not continue to rise with forcing in Regime C. Runs at higher forcings (not shown) have approximately the same mean flow extraction by $m2$ as for $\Delta T^\dagger = 90$ K. This confirms that $m2$ has reached its (constant) heat transport threshold in Regime C.

The relative importance of the nonlinear transfer within Regimes T and C is of interest here. Comparing Panels T and C, we see that as the forcing is increased, the quasi-linear extraction by the dominant mode grows significantly; however, the nonlinear transfer increases much less. Further tests at $\Delta T^\dagger > 90$ K (not shown) yield the same effect: for a slight increase in forcing there is a corresponding increase in quasi-linear extraction of energy from the mean flow, while the nonlinearities remain roughly unchanged. Therefore, the system becomes more and more quasi-linear as the forcing is raised. We note that Cehelsky and Tung (1991) also found their model to be nearly quasi-linear at high drivings. This is also demonstrated in a different manner in Fig. 4: as the forcing is raised, the heat transport by $m2$ becomes less and less significant compared with that by $m1$.

We are also concerned with the role of nonlinear transfer in *evolving* to equilibrium. In section 4b we showed that the wave breaking process in Regime T is crucial to the evolution and that the process is nonlinear by definition. In Regime C, the wavenumber selection process is qualitatively the same as in Regime T. In fact, this can be seen right from the initial linear stability curve of Fig. 1. Some nonlinear processes must come into play in the selection of $m1$; otherwise the most unstable mode $m2$ would simply dominate from the start.

Our findings contrast with the work of Cai (1992). We have found that nonlinear interactions are necessary in maintaining the equilibrium for moderate forcings, which contradicts his use of a quasi-linear model to determine the equilibrium state. Our results *do* agree with Cai that at low forcings equilibrium is maintained effectively quasi-linearly. However, at high forcings, another regime in which our model is approximately quasi-linear, Cai's method would select the wrong wave as dominant. This was demonstrated by applying his method to the present model, that is, by comparing quasi-linear runs with $m1$ perturbed to those with $m2$ perturbed. The equilibrated temperature gradient is lower when $m2$ is perturbed than $m1$ at every forcing (not shown); thus Cai's theory would predict that $m2$ would dominate always! This is obviously not the result found here, nor that observed in the real atmosphere. Thus, we only agree with Cai's method and theory for weak forcings, that is, Regime B.

It would be of interest to compare the behavior observed here to theories of geostrophic turbulence, in particular the Rhines (1975) wavenumber of cascade arrest and Salmon's (1980) "wave–wave equilibration" process (see also Vallis 1988). While there is a correspondence, we delay detailed discussion to the more relevant case when there are many waves unstable (Welch and Tung 1998), so that the same part of parameter space is being investigated.

We now return to an interesting point mentioned earlier in this section: even at equilibrium in Regime C,

wavenumber 2 is linearly *un*stable. This is seen in Fig. 2, for $\Delta \overline{T}_{eq} > \Delta \overline{T}_{cr,m2}$ at every level of forcing in Regime C. How can a wave be unstable at equilibrium? The answer is that this wave is stabilized by a different process than simple (quasi)linear dynamics. Wavenumber 2 does indeed interact quasi-linearly with the mean flow, but it is stabilized via nonlinear saturation, by sending excess energy to longer-scale waves. Thus wavenumber 2 can have a positive linear growth rate even at equilibrium. Meanwhile, wavenumber 1 is stabilized quasilinearly: it interacts strongly with and modifies the mean flow until the mean flow is neutral with respect to it. In contrast to $m2$, $m1$ will have a zero linear growth rate at equilibrium, as shown in Fig. 2.

Note that the equilibration mechanism found here is not one of neutralization, as has been proposed by Lindzen (1993, 1994), which in our opinion is too severe a condition. It is not necessary to neutralize the zonal mean atmosphere to all waves for it to equilibrate; it only needs to be neutral to the dominant wave. The linearly most unstable wave is usually stabilized via nonlinear transfer. Thus a *linear* theory of neutralization is insufficient to explain the equilibration.

We also point out that our model includes both normal modes and nonmodal waves. The results, however, can be interpreted using modal instability only. The transient growth mechanisms presented by Farrell and Ioannou (1995) and DelSole and Farrell (1996) do not appear necessary to explain this problem, in which we examine the long-term evolution to equilibrium.

6. Details of the equilibrium

A few details of the equilibrium deserve some comment. There is only a little barotropic shear introduced into the zonal velocities in the process of equilibration (not shown). The primary stabilization of the flow, therefore, does not appear to be due to the barotropic governor effect (James 1987) in which a large meridional shear develops and reduces the growth rate of baroclinic waves. (Note that the linear stability analysis performed previously includes any barotropic instability that might exist and hence any barotropic governor effect.) Also, the zonal velocities in the lower layer are very small and hence unlike the real atmosphere. These small values are due to two effects: first, the fact that the side walls are assumed to be rigid, which prevents zonal momentum fluxes from propagating into or out of the channel, thereby ensuring a channel-averaged zonal velocity near zero at the surface (Tung and Rosenthal 1985); second, the formulation of the lower boundary condition. For the latter we used $\Psi_4 \approx \Psi_3$ in assigning ω_4 (see section 2b). We tested this approximation by using $\Psi_4 \approx (3/2)\Psi_3 - (1/2)\Psi_1$ instead (derived from the hydrostatic equation), but the model simulations remain qualitatively the same. While the equilibrated lower-layer flows are indeed larger with this new approximation, a shift to the longer wave still occurs as
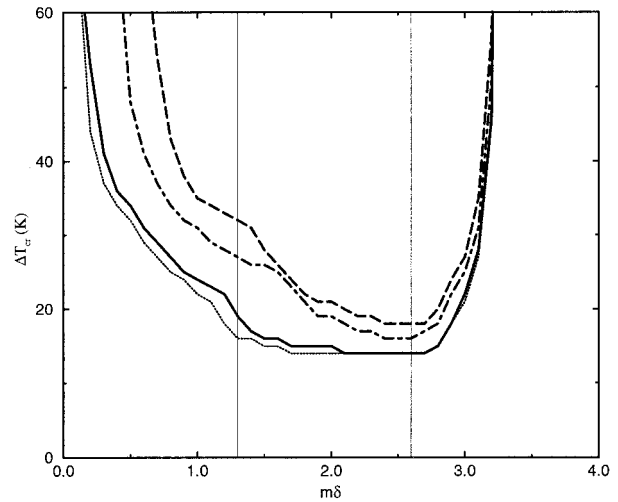

FIG. 9. As in Fig. 1 but for several values of the Newtonian cooling parameter h'': 6-day *e*-folding time (dashed line), 11 days (dot-dashed), 56 days (solid, the curve of Fig. 1), and 112 days (dotted). Thin vertical lines are at $m = 1$ and $m = 2$ for the geometry $\delta = 1.3$.

the forcing is raised, there is little barotropic shear introduced into the flow, and the equilibration is still critical relative to the dominant heat transporting wave. Thus the unrealistically small lower-layer velocities in the original formulation do not seem to be important.

We should point out that the mechanism described here occurs at other values of δ as well, for which more than two waves are initially unstable. There is always a shift from the short, most unstable wave to a longer wave, which dominates the heat transport at equilibrium, for all but the lowest forcings. In particular, this mechanism is demonstrated in a realistic simulation in Welch and Tung (1998).

The model results do have some sensitivity to the value chosen for the Newtonian cooling parameter h''. In general, a model with a longer thermal damping time is more unstable, as confirmed in Fig. 9 with marginal stability curves for several values of h''. This allows the flow to evolve further from the radiatively forced state of (2.6)–(2.7), and for more heat transport by each wave and hence a lower equilibrated temperature gradient (all not shown). However, these features by themselves are not particularly interesting. Note also that a longer thermal damping time does not allow the flow to evolve further from criticality. Regardless of the value of h'', the flow at each forcing equilibrates near the critical gradient for the dominant heat transporting wave in the modified flow.

There is, in fact, a significant effect of varying h'': a *differential* impact on waves of different scale. Specifically, as h'' is lowered, $m1$ is increasingly unstable while $m2$'s instability is less affected; thus the two waves have closer and closer critical gradients as h'' is decreased (see Fig. 9). One might expect that $m1$ would be more involved in the heat transport for a lower value of h'', that is, that $m1$ would begin to be the dominant wave

at lower forcings. However, recall from section 3b that the dividing line between Regimes B and T is not determined by $\Delta\overline{T}_{cr,m1}$ but rather by the heat transport threshold of $m2$. This threshold, in fact, *increases* as h'' decreases, and hence $m1$ becomes involved in the heat transport at *higher* forcings for lower values of h''.

The above is the main effect of varying h''. It is a quantitative difference only, affecting the size of the various forcing regimes but not their existence. Our conceptual model of baroclinic adjustment is independent of this thermal damping parameter. To demonstrate the mechanism, therefore, we have chosen a value for h'' that is smaller than is realistic, but for which each regime of Fig. 5 is discernible in output such as Figs. 2 and 4.

7. Summary

In this work we have performed a detailed study of the mechanism of nonlinear baroclinic adjustment. We have seen that baroclinically equilibrated flows are robust in several measures; the cross-channel temperature gradient, the zonal mean PV and its meridional gradient, and the potential enstrophy in each layer are all roughly constant for a wide range of forcings. Moreover, the mechanism of nonlinear baroclinic adjustment, including a nonlinear wavenumber selection process, can explain equilibration over this wide forcing range.

In the wavenumber selection part of the mechanism, the shorter, linearly most unstable wave has a threshold of heat transport, above which it renders the fluid state unstable to secondary perturbations. When the forcing is low, the shorter wave never reaches this threshold and thus it, as the most unstable wave, dominates the heat transport at equilibrium. For higher forcings, the shorter wave will reach its threshold and will not be able to transport further heat. It will cease its growth by breaking, passing its energy to the still unstable longer wave through nonlinear transfer. This process is called saturation. The longer wave will transport the extra heat required to achieve the robust equilibrium. (There is also a threshold of heat transport for the longer wave, but it is much higher than that for the shorter wave.) If the forcing is high enough, the excess heat transported by the longer wave will exceed that of the shorter wave, which is capped at its threshold, and the longer wave will dominate. A procedure is outlined that will allow a predictive formula to be developed to calculate when each wave will break.

The maintenance of the equilibrium is fairly simple once the dominant heat transporting wave has been selected, and in most cases it is surprisingly quasi-linear considering the large supercriticality. The dominant wave transports heat poleward, reducing the overall temperature gradient and adjusting the mean flow meridionally, until the flow reaches a state that is linearly critical relative to the dominant wave. This is a process of critical equilibration; the dominant wave stabilizes itself, that is, quasi-linearly. For high forcings, this quasi-linear equilibration is done by the longer wave. The shorter wave then is stabilized by a different process: nonlinear transfer of energy to other modes.

REFERENCES

Andrews, D., J. Holton, and C. Leovy, 1987: *Middle Atmosphere Dynamics.* Academic Press, 489 pp.

Cai, M., 1992: An analytic study of the baroclinic adjustment in a quasigeostrophic two-layer channel model. *J. Atmos. Sci.,* **49,** 1594–1605.

Cehelsky, P., 1987: Multiple equilibria, weather regimes and nonlinear equilibration in a simple baroclinic model. Ph.D. thesis, Massachusetts Institute of Technology, 161 pp.

——, and K. Tung, 1987: Theories of multiple equilibria and weather regimes—A critical reexamination. Part II: Baroclinic two-layer models. *J. Atmos. Sci.,* **44,** 3282–3303.

——, and ——, 1991: Nonlinear baroclinic adjustment. *J. Atmos. Sci.,* **48,** 1930–1947.

Charney, J., and M. Stern, 1962: On the stability of internal baroclinic jets in a rotating atmosphere. *J. Atmos. Sci.,* **19,** 159–172.

Chou, S., 1995: Wavenumber selection and hysteresis in nonlinear baroclinic flows. *J. Atmos. Sci.,* **52,** 3236–3246.

Cubasch, U., K. Hasselmann, H. Hock, E. Maier-Reimer, U. Mikolajewicz, B. Santer, and R. Sausen, 1993: Time-dependent greenhouse warming computations with a coupled ocean–atmosphere model. *Climate Dyn.,* **8,** 55–69.

DelSole, T., and B. Farrell, 1996: The quasi-linear equilibration of a thermally maintained, stochastically excited jet in a quasigeostrophic model. *J. Atmos. Sci.,* **53,** 1781–1797.

Farrell, B., and P. Ioannou, 1995: Stochastic dynamics of the midlatitude atmospheric jet. *J. Atmos. Sci.,* **52,** 1642–1656.

Gall, R., 1976: A comparison of linear baroclinic instability theory with the eddy statistics of a general circulation model. *J. Atmos. Sci.,* **33,** 349–373.

——, R. Blakeslee, and R. Somerville, 1979: Baroclinic instability and the selection of the zonal scale of the transient eddies of middle latitudes. *J. Atmos. Sci.,* **36,** 767–784.

Garcia, R. R., 1991: Parameterization of planetary wave breaking in the middle atmosphere. *J. Atmos. Sci.,* **48,** 1405–1419.

Gutowski, W., L. E. Branscome, and D. Stewart, 1989: Mean flow adjustment during life cycles of baroclinic waves. *J. Atmos. Sci.,* **46,** 1724–1737.

Haidvogel, D., and I. Held, 1980: Homogeneous quasi-geostrophic turbulence driven by a uniform temperature gradient. *J. Atmos. Sci.,* **37,** 2644–2660.

Hart, J., 1981: Wavenumber selection in nonlinear baroclinic instability. *J. Atmos. Sci.,* **38,** 400–408.

Held, I., 1978: The vertical scale of an unstable wave and its importance for eddy heat flux parameterizations. *J. Atmos. Sci.,* **35,** 572–576.

Holton, J., 1979: *An Introduction to Dynamic Meteorology.* 2d ed. Academic Press, 391 pp.

James, I., 1987: Suppression of baroclinic instability in horizontally sheared flows. *J. Atmos. Sci.,* **44,** 3710–3720.

Klein, P., and J. Pedlosky, 1986: A numerical study of baroclinic instability at large supercriticality. *J. Atmos. Sci.,* **43,** 1243–1262.

Lindzen, R., 1990: *Dynamics of Atmospheric Physics.* Cambridge University Press, 310 pp.

——, 1993: Baroclinic neutrality and the tropopause. *J. Atmos. Sci.,* **50,** 1148–1151.

——, 1994: The Eady problem for a basic state with zero pv gradients but $\beta \neq 0$. *J. Atmos. Sci.,* **51,** 3221–3226.

Lorenz, E., 1960: Energy and numerical weather prediction. *Tellus,* **12,** 364–373.

——, 1963: The mechanics of vacillation. *J. Atmos. Sci.,* **20,** 448–464.

Maier-Reimer, E., U. Mikolajewicz, and K. Hasselmann, 1993: Mean circulation of the Hamburg LSG OGCM and its sensitivity to the thermohaline surface forcing. *J. Phys. Oceanogr.,* **23,** 731–757.

Mak, M., 1985: Equilibrium in nonlinear baroclinic instability. *J. Atmos. Sci.,* **42,** 2764–2782.

Manabe, S., and R. Stouffer, 1988: Two stable equilibria of a coupled ocean–atmosphere model. *J. Climate,* **1,** 841–866.

——, and ——, 1993: Century-scale effects of increased atmospheric CO_2 on the ocean–atmosphere system. *Nature,* **364,** 215–218.

——, ——, M. Spelman, and K. Bryan, 1991: Transient responses of a coupled ocean–atmosphere model to gradual changes of atmospheric CO_2. *J. Climate,* **4,** 785–817.

McIntyre, M., and T. Palmer, 1983: Breaking planetary waves in the stratosphere. *Nature,* **305,** 593–600.

——, and ——, 1984: The ''surf zone'' in the stratosphere. *J. Atmos. Terr. Phys.,* **46,** 825–849.

Pedlosky, J., 1981: The nonlinear dynamics of baroclinic wave ensembles. *J. Fluid Mech.,* **102,** 169–209.

Phillips, N., 1954: Energy transformations and meridional circulations associated with simple barclinic waves in a two-level, quasi-geostrophic model. *Tellus,* **6,** 273–286.

Randel, W., and I. Held, 1991: Phase speed spectra of transient eddy fluxes and critical layer absorption. *J. Atmos. Sci.,* **48,** 688–697.

Rhines, P., 1975: Waves and turbulence on a beta-plane. *J. Fluid Mech.,* **69,** 417–443.

Salmon, R., 1980: Baroclinic instability and geostrophic turbulence. *Geophys. Astrophys. Fluid Dyn.,* **15,** 167–211.

Stone, P., 1978: Baroclinic adjustment. *J. Atmos. Sci.,* **35,** 561–571.

——, and D. Miller, 1980: Empirical relations between seasonal changes in meridional temperature gradients and meridional fluxes of heat. *J. Atmos. Sci.,* **37,** 1708–1721.

——, and J. Risbey, 1990: On the limitations of general circulation climate models. *Geophys. Res. Lett.,* **17,** 2173–2176.

Tung, K., 1983: On the nonlinear versus linearized lower boundary conditions for topographically forced stationary long waves. *Mon. Wea. Rev.,* **111,** 60–66.

——, and A. Rosenthal, 1985: Theories of multiple equilibria—A critical reexamination. Part I: Barotropic models. *J. Atmos. Sci.,* **42,** 2804–2819.

——, and ——, 1986: On the extended-range predictability of large-scale quasi-stationary patterns in the atmosphere. *Tellus,* **38A,** 333–365.

Vallis, G., 1988: Numerical studies of eddy transport properties in eddy resolving and parameterized models. *Quart. J. Roy. Meteor. Soc.,* **114,** 183–204.

Washington, W., and G. Meehl, 1989: Climate sensitivity due to increased CO_2: Experiments with a coupled atmosphere and ocean general circulation model. *Climate Dyn.,* **4,** 1–38.

Welch, W. T., 1996: Nonlinear baroclinic adjustment and wavenumber selection as a mechanism for atmospheric heat transport. Ph.D. thesis, University of Washington, 131 pp.

——, and K. Tung, 1998: On the equilibrium spectrum of transient waves in the atmosphere. *J. Atmos. Sci.,* in press.

Whitaker, J., and A. Barcilon, 1995: Low-frequency variability and wavenumber selection in models with zonally symmetric forcing. *J. Atmos. Sci.,* **52,** 491–503.

Zhou, S., and P. H. Stone, 1993: The role of large-scale eddies in the climate equilibrium. Part II: Variable static stability. *J. Climate,* **6,** 1871–1881.